

# Study of liquid metal surface wave damping in the presence of magnetic fields and electrical currents

A.E. Fisher, M.G. Hvasta, E. Kolemen

Department of Mechanical and Aerospace Engineering, Princeton University, Princeton, NJ, USA



## ARTICLE INFO

**Keywords:**  
Liquid metal  
Lorentz force  
Surface waves

## ABSTRACT

Experiments and predictions of surface wave damping in liquid metal due to a surface aligned magnetic field and externally regulated  $j \times B$  force are presented. Fast-flowing, liquid-metal plasma facing components (LM-PFCs) are a proposed alternative to solid PFCs that are unable to handle the high heat flux, thermal stresses, and radiation damage in a tokamak. The significant technical challenges associated with LM-PFCs compared to solid PFCs are justified by greater heat flux management, self-healing properties, and reduced particle recycling. However, undesirable engineering challenges such as evaporation and splashing of the liquid metal introduce excessive impurities into the plasma and degrade plasma performance. Evaporation may be avoided through high-speed flow that limits temperature rise of the liquid metal by reducing heat flux exposure time, but as flow speed increases the surface may become more turbulent and prone to splashing and uneven surfaces. Wave damping is one mechanism that reduces surface disturbance and thus the chances of liquid metal impurity introduction into the plasma. Experiments on the Liquid Metal eXperiment Upgrade (LMX-U) examined damping under the influence of transverse magnetic fields and vertically directed Lorentz force.

## 1. Introduction

### 1.1. Motivation and background

Liquid-metal surface stability and wave damping due to magnetic fields and Lorentz force has been previously evaluated theoretically [1,2] and experimentally [3–5]. These derivations and experiments show that both the direction of the magnetic field with respect to surface waves, as well as the presence of externally injected electrical currents that generate a Lorentz (or  $j \times B$ ) force given by (1) are key factors that govern the behavior of surface waves.

$$\vec{F}_L = \vec{j} \times \vec{B} \quad (1)$$

Specifically, anisotropic damping is predicted to occur such that surface-aligned magnetic fields contribute to wave damping only when oriented parallel to the direction of wave propagation [1,2].

Many experiments have taken interest in liquid metal waves, splashing stability limits, and stabilizing forces regarding liquid-metal plasma facing components (LM-PFCs) [3–9]. Of the experiments that examined surface wave behavior, they observed the predicted anisotropic wave damping where surface perturbations traveling the direction of the magnetic field quickly vanish, and evaluate surface stability limits under  $j \times B$  force. These experimental observations of wave

damping and fluid behavior have shown consistent results, but have been limited to weak magnetic fields, lack of external electrical current, and/or provide only qualitative evidence of the anisotropic wave damping.

The governing equations and derivation of the dispersion relations for the waves examined may be found in Appendix A, accompanied by explanation of the consequences of the results and predictions of wave behavior. Testing in the LMX-U channel aims to verify these predictions by examining surface waves propagating perpendicular to a magnetic field with and without externally injected electrical currents to induce vertically directed  $j \times B$  force ( $\pm j_{0,x}B_z$ ).

## 2. Experimental setup

LMX-U is a free-surface liquid-metal channel flow test loop at the Princeton Plasma Physics Laboratory (PPPL). LMX-U uses a GaInSn eutectic alloy of 67% gallium, 20.5% indium, 12.5% tin as the working liquid-metal due to its fluidity at room temperature, low reactivity, and non-toxic properties. During LMX-U operation, a gear pump circulates the liquid-metal using a rotary gear pump through an argon-inerted, acrylic-walled channel equipped with diagnostics. For the experiments presented in this paper the channel is not flowing, and depth is kept constant by valving off back-flow, along with installing a weir at the

E-mail address: [aefisher@princeton.edu](mailto:aefisher@princeton.edu) (A.E. Fisher).

<https://doi.org/10.1016/j.nme.2019.02.014>

Received 15 August 2018; Received in revised form 1 February 2019; Accepted 11 February 2019  
2352-1791/© 2019 Published by Elsevier Ltd. This is an open access article under the CC BY-NC-ND license (<http://creativecommons.org/licenses/by-nc-nd/4.0/>).

**Nomenclature**

Variable	Symbol and Units
Flow velocity	$u$ [m/s]
Galinstan density	$\rho$ [kg/m <sup>3</sup> ]
Magnetic field	$B$ [T]
Electrical current	$j$ [A/m <sup>2</sup> ]
Pressure	$p$ [Pa]
Electric field	$E$ [V/m]
Surface tension	$T$ [N/m]

Electrical conductivity	$\sigma$ [S/m]
Wave amplitude	$a$ [m]
Wave number	$k$ [m <sup>-1</sup> ]
Wave frequency	$\omega$ [s <sup>-1</sup> ]
Liquid depth	$h$ [m]
Time	$t$ [s]
Gravity	$g$ [m/s <sup>2</sup> ]
Viscosity	$\mu$ [Pa s]
MHD drag force	$F_D$ [N/m <sup>3</sup> ]
Wave phase velocity	$u_{ph}$ [m/s]

outlet.

Fusion reactors are unlikely to use a GaInSn alloy as a working liquid-metal, and may instead use lithium due to favorable plasma-confinement properties and being a relatively benign impurity [10,11]. Projecting to lithium shows a significant drawback of using a GaInSn alloy as a working fluid, as lithium is less than 8% the density—however the electrical conductivity of the two are comparable near an operating temperature of 50 °C for liquid lithium [12]. The positive aspect of the difference in density is that when extrapolating to a reactor using liquid-lithium PFCs, any favorable effects of added Lorentz force may be obtained at far lower externally injected electrical currents and/or magnetic fields as lithium is more easily accelerated.

As depicted in Fig. 1 the complete channel length is  $L \approx 125$  cm, within a C-shaped electromagnet beginning  $\approx 29$  cm from the inlet edge, and spanning  $\approx 74$  cm of the channel length. A more detailed description of the experimental capabilities and diagnostics used can be found in past work [13]. An argon cover-gas is used to reduce oxidation of the liquid-metal by slowly but continuously pushing pressurized argon through a hose connected to a brass port near the channel inlet and venting through another brass port and hose near the outlet. The pressure within the channel can be kept slightly above atmospheric, up to  $\approx 2$ [psi] gage. Under positive gage pressure, the flexible plastic piping in the system expands slightly, causing a small amount of

liquid-metal to flow back into the inlet hose. This amount is negligible compared to the total system capacity. By creating a sudden pressure drop in the cover gas to zero gage via rapid gas venting, the plastic piping contracts and pushes the liquid-metal back into the channel. The liquid-metal pushed back into the channel comes vertically upwards at the inlet through a rectangular hole, generating a wave. This mechanism was used to generate small-amplitude waves within the channel for measurement.

An overhead camera was used to record wave motion in the channel. The wave position is determined by tracking distortions in the reflected image off of the fluid surface. Three frames from an overhead video of a wave traveling down the channel can be seen in Fig. 2.

A sliding laser sheet and camera were used to take depth measurements at different points in the channel. Details on the operation of this diagnostic are described in past work [13,14]. Fig. 3 shows a wave traveling under the laser sheet, with the magnetic field and externally injected electrical current indicated by arrows. A first-order temporal decay predicted the peak amplitude of the initial wave as it reflected back and forth in the channel past the laser sheet. The fit used to determine an average decay timescale is shown in (2).

$$a = a_0 e^{t/\tau_c} \tag{2}$$

Comparing data across the same experimental conditions confirmed

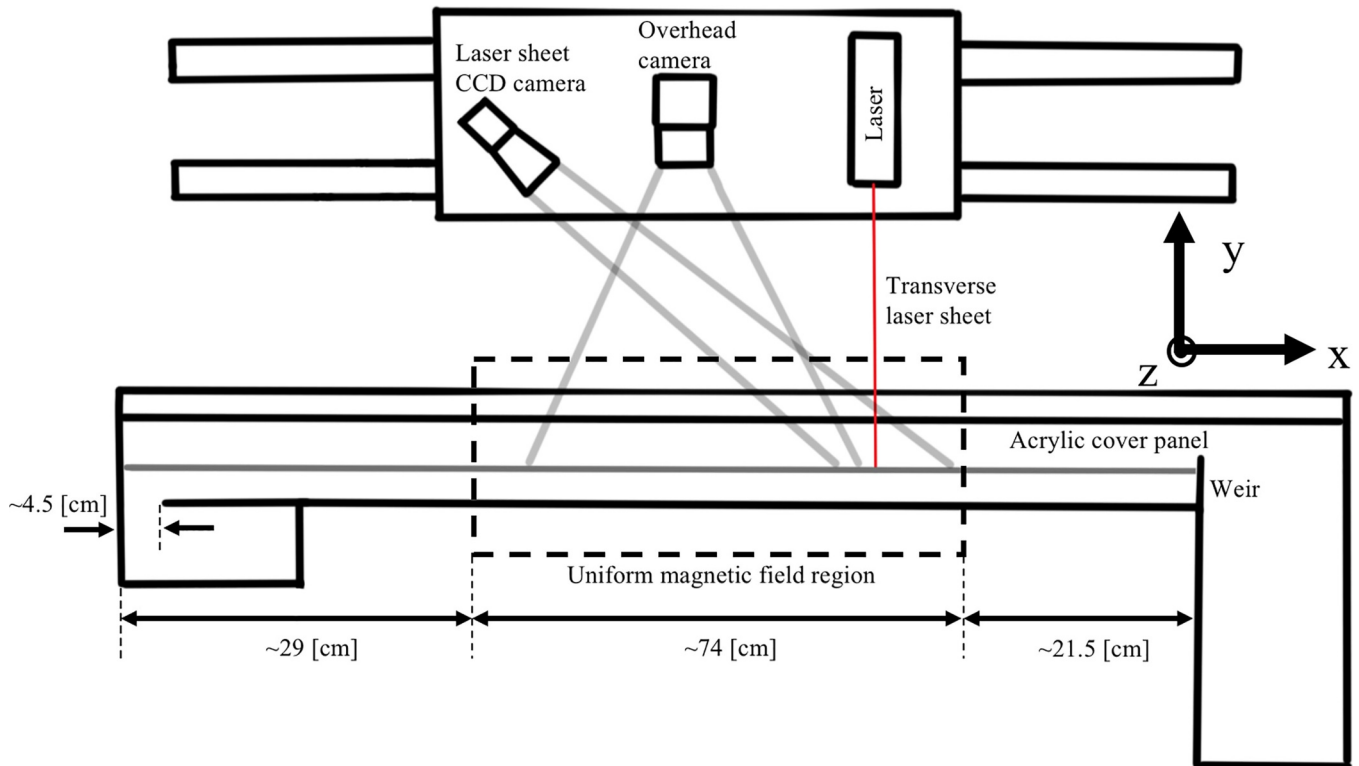


Fig. 1. Schematic of the LMX-U channel with diagnostics and dimensions shown—not to scale.

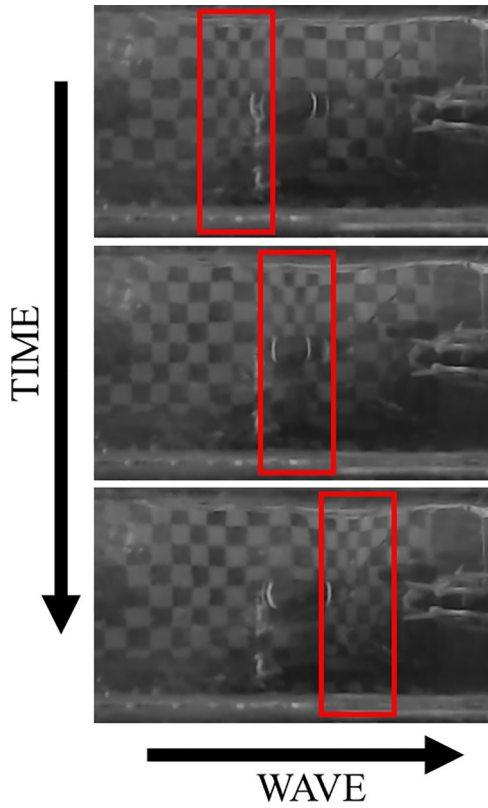


Fig. 2. Three frames from an overhead video of a wave traveling down the channel. The checkerboard image distortions caused by the wave are marked by red boxes. The frames are spaced by  $\approx 0.1$  s each. (For interpretation of the references to colour in this figure legend, the reader is referred to the web version of this article.)

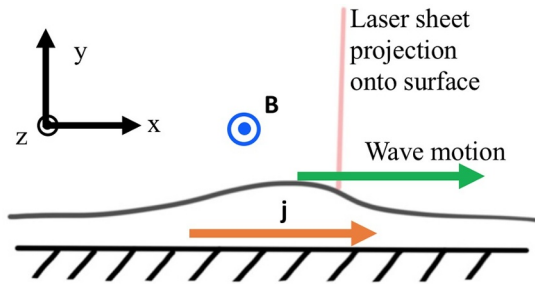


Fig. 3. Schematic of a traveling wave under the laser sheet diagnostic. The shown magnetic field direction is fixed on LMX-U (positive z-direction), while the electrical current direction may be reversed—causing in a reversal in direction of the resultant Lorentz force.

the repeatability of the wave generation method used in this study. The details of the findings from this data is discussed in Section 3.

### 3. Methods and results

Waves were generated in the LMX-U channel using the pressure drop method discussed in Section 2. For the data shown, each channel location and magnetic field/electrical current configuration was tested eight times with experimental conditions held constant. The sliding laser sheet and camera were used to take wave amplitude measurements at four channel locations within the uniform magnetic field region, each separated by 15 cm. Waves between tests had no qualitative differences and were mostly indistinguishable from each other. Peak depths could vary slightly; this is mostly attributed to the camera frame rate (15 fps) being too low to consistently capture the peak wave depth.

#### 3.1. Wave amplitude change due to magnetic field

A total of five magnetic field strengths ranging up to 0.33 T were evaluated. The wave amplitudes measured were normalized against the initial measured wave peak in the zero magnetic field case (Fig. 4A), as well as the initial measured wave peak in each respective magnetic field case (Fig. 4B). The depth of the channel was measured to be  $\approx 7.8$  mm, and with the wavenumber determined from measurement to be  $\approx 22$   $\text{m}^{-1}$ , the shallow approximation holds as  $\tanh(kh) \approx kh$  within several percent.

Increases in wave damping along the channel length are not observed, as all the normalized amplitudes in Fig. 4 B are not predictably ordered by magnetic field, are comparable in slope, and are within error bars. However, the data shown in Fig. 4 A is consistently shifted downwards as magnetic field is increased, indicating a change in the initial wave amplitude before reaching the first measurement location. An explanation for this shift can be attributed to the wave traveling a short distance outside the uniform field where propagation-aligned field lines damp the waves at different levels depending on field strength [2,4].

A FEMM simulation was used to model the propagation aligned magnetic field component ( $B_x$ ) in the channel, including outside the C-shaped magnet bounds [15]. The propagation-aligned field was found to be zero within the majority of the electromagnet air gap as expected, with the value of  $B_x^2$  (the relevant quantity for damping) reaching a spanwise-averaged maximum of  $\approx 1.7\%$  of the value of  $B_z^2$  just outside the air gap— $B_x^2$  then proceeds to decay to less than 3% of its maximum value at either edge.

By modeling the amplitude decay according to (3) with the solution (4), and integrating along the inlet region leading up to where  $B_x = 0$ , it was found that the shift seen in Fig. 4 could be predicted by scaling the convective damping rate in (A.8) by a constant  $c_{k_i}$  (surface tension effects were ignored due to being relatively small compared to  $\rho\omega^2$ ). The term  $k_{\text{visc}}$  was determined by matching the integrated amplitude to the weak magnetic field case, while the initial amplitude  $a_0$  was found by extrapolating the amplitude trend seen in Fig. 6 to the channel inlet.

$$\frac{\partial a}{\partial x} = -a \left( c_{k_i} \frac{\sigma B_x^2}{2\rho u_{ph}} + k_{\text{visc}} \right) \quad (3)$$

$$a = a_0 e^{(k_i + k_{\text{visc}})x} = a_0 e^{-\left( c_{k_i} \frac{\sigma B_x^2}{2\rho u_{ph}} + k_{\text{visc}} \right)x} \quad (4)$$

Using (A.8) without scaling overpredicts the damping seen—this is expected as the waves examined were close to the shallow limit where no damping is predicted [4]. The predicted amplitude shift between the data sets is shown in Fig. 5.

By using the contributions to decay rate found from Fig. 5, an amplitude prediction was made for the wave as it reflected back and forth in the channel shown in Fig. 6. It is seen in the predicted peak amplitude that there is a non-uniform decay rate due to more damping taking place in the fringing field regions. The wave amplitude is slightly overpredicted; a possible explanation is the non-uniformity of oxides on the surface may have lead to more damping than could be predicted from only the inlet length [4]. Furthermore, comparing the shape of amplitude decay to that in Fig. 6 shows a distinct difference in curvature. One factor is the aforementioned surface oxides that lead to uneven damping across the channel length. In addition, it only takes  $\approx 1.5$  s for the wave to traverse all four measurement locations, so the expected change is close to linear. Another decay rate can be seen in Fig. 6 after each marked peak measurement. This observed decay is a product of the wave generation mechanism creating smaller waves following the original, and does not offer useful information for this study.

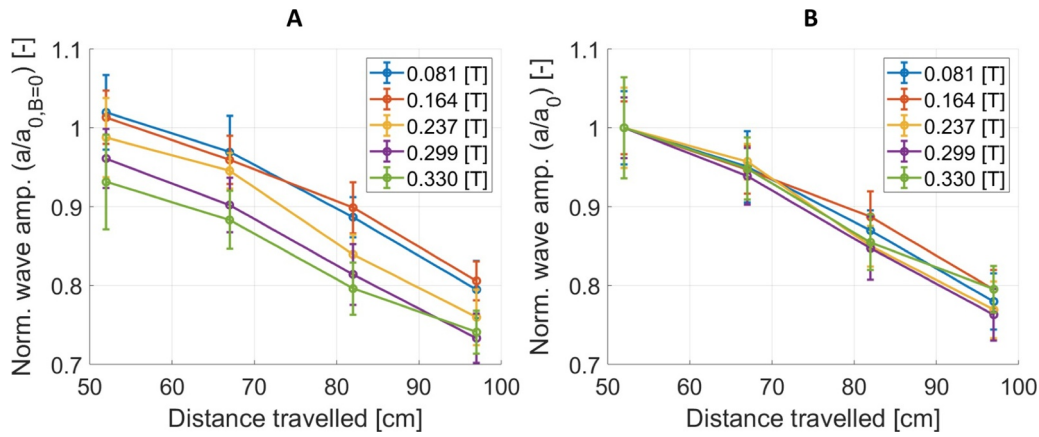


Fig. 4. Normalized wave amplitudes along the length of the channel. Wave amplitudes plotted in A are normalized by the initial amplitude in the zero magnetic field case. Wave amplitude plotted in B are normalized by the initial amplitude of each respective magnetic field strength.

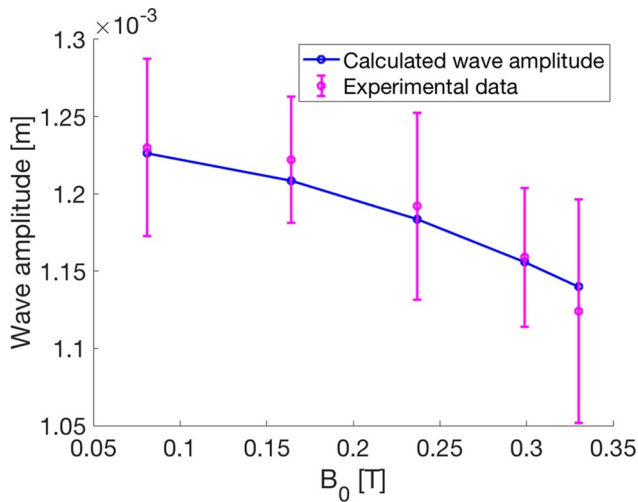


Fig. 5. Wave amplitude measurements and predictions at the first (52 cm travelled) position from Fig. 4. The prediction shown accounted for both non-magnetic field losses, and 45% of the predicted loss given from the convective damping rate given by (A.8) with surface tension neglected.

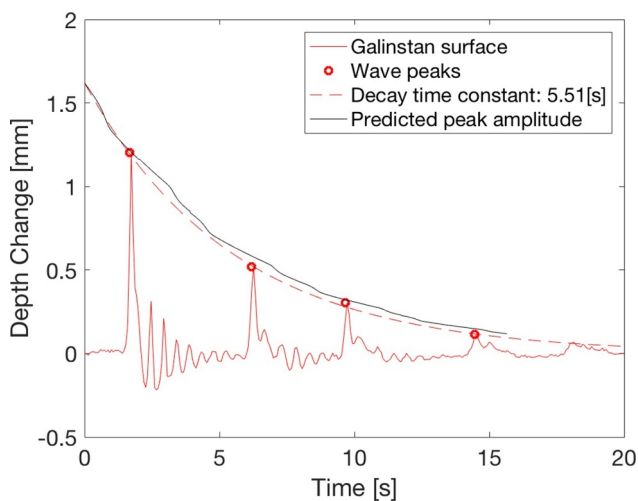


Fig. 6. Temporal channel depth changes measured at a single location as the wave reflected back and forth in the LMX-U channel in the  $B = 0.299$  T case. A prediction of the amplitude of the initial wave in time is provided based on the findings from Fig. 5.

### 3.2. Wave amplitude change due to magnetic field with $j \times B$ force

Two externally injected current configurations were investigated that resulted in a  $j \times B$  force either parallel or anti-parallel to gravity. Given the fluid cross-section of  $A \approx 8.5$  cm<sup>2</sup>, the current density is  $j = I/A \approx 130,000$  A/m<sup>2</sup>. With the magnetic field strength at 0.276 T, the resultant force is  $j \times B \approx 36,000$  N/m<sup>3</sup>—slightly more than half that of gravity ( $\rho g \approx 64,000$  N/m<sup>3</sup>). The wave amplitudes measured were normalized against the initial measured wave peak in the  $B = 0.276$  T,  $I = 0$  A case. The measured normalized amplitudes are shown in Fig. 7. The two cases are nearly a linear scaling of one another, indicating no significant difference in wave amplitude decay rate. When examining the amplitude difference, the case with the downward pointing Lorentz force case had a larger wave amplitude. This is not explained through the previous fringing field analysis as both cases were exposed to the same magnetic field. Instead, this shift is likely attributed to change in fluid depth within the test section.

As shown in [14,16], the liquid-metal depth is lowered or raised in the uniform  $j \times B$  force region relative to the  $j \times B = 0$  region—causing the wave to either enter shallower or deeper flow depending on the direction of  $j \times B$ . Eliminating this from the experiments was difficult as the waves were generated outside of the uniform  $j \times B$  region, so the uniform  $j \times B$  region could not be isolated from the rest of the pool. At this shallow limit the depth change is difficult to predict due to the increased importance of surface tension not accounted for in [14].

One possible explanation for the difference in wave amplitude is similar to the growth of a wave as it travels into increasingly shallow

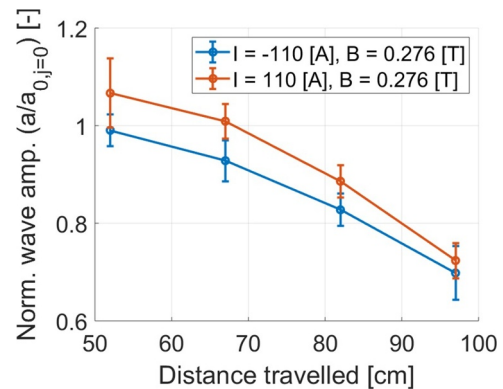


Fig. 7. Normalized wave depth along the channel length under  $j \times B$  force. Negative electrical current implies resultant force opposing gravity while positive electrical current implies resultant force adding to gravity. The wave amplitude is normalized by the initial amplitude in the zero electrical current case.

water, like a tsunami approaching the coast. The wave in the case of  $j \times B$  force directed downwards moves into shallower conditions, and has a larger amplitude than that of the  $j \times B$  force directed upwards case which moves into deeper fluid. The anticipated wave amplitude based on the change in depth is governed by (5) [17].

$$a = a_0(d_0/d)^{1/4} \quad (5)$$

Conditions in LMX-U differ from traditional application of (5) as the channel bottom remains horizontal while the rising/falling of fluid surface is what is changing the depth—rather than the fluid surface remaining horizontal and the channel bottom rising/falling. Applying this equation to the amplitude shift seen in Fig. 7 only predicts  $\approx 33\%$  of the wave growth seen between the  $j \times B$  up and  $j \times B$  down cases. This suggests that there are further effects not being accounted for or that the depth changes are too sudden to apply (5) properly [17].

#### 4. Summary and outlook

Transverse magnetic fields perpendicular to wave propagation both with and without externally injected electrical currents to induce  $j \times B$  force were shown to have no effect on wave damping in the investigated parameter space. This result confirms predictions from theory and expands the parameter space of previous experiments [4]. Additionally, surface wave damping due to the fringing field outside of uniform magnetic field region was evaluated.

Further work is needed to examine the behavior of higher wave number waves, as well as waves with different boundary conditions. Higher wave numbers experience stronger stabilizing forces from surface tension, and eventually deviate from the shallow-limit. Conductive boundary conditions or axisymmetric boundary conditions will more closely match reactor-like conditions, and may exhibit different wave behavior.

##### 4.1. Projecting to fusion reactors

Fast-flowing thin-film divertors have known challenges associated with the substantial losses due to MHD drag [18]. Additional challenges come from the magnetic field gradients that may be used for magnetic propulsion, but can also lead to flow piling and splashing [19,20].

Wave damping due to the ambient magnetic field can help eliminate these instabilities. Assuming a fast-flowing liquid metal divertor will flow on the order of 10 m/s over a 10 cm region, the flow exposure timescale is on the order of 0.01 s. Examining (4), the exponent may be multiplied by the wave velocity  $u_{ph}$  to obtain a temporal decay rather

#### Appendix A. Governing equations and dispersion relations

Linear MHD surface wave theory is governed by the MHD equations for incompressible flow shown in (A.1) and (A.2).

$$\nabla \cdot \vec{u} = 0 \quad (A.1)$$

$$\rho(\partial \vec{u} / \partial t + (\vec{u} \cdot \nabla) \vec{u}) = \rho \vec{g} - \nabla p + \vec{j} \times \vec{B} + \mu \nabla^2 \vec{u} \quad (A.2)$$

$$\vec{j} = \sigma(\vec{E} + \vec{u} \times \vec{B}) \quad (A.3)$$

$$\nabla \cdot \vec{j} = 0 \quad (A.4)$$

A useful distinction for the sources of electrical current given by (A.3) is recasting  $\vec{j}$  as  $j = j_0 + j_1$ , where  $j_0$  captures the externally injected electrical currents via electrodes and  $j_1$  results from the motion of the liquid metal within the magnetic field. Looking at the flow-opposing drag force predicted by  $j_1$ , the induced current term in (A.3) can be substituted in (1) to find scaling according to relation (A.5). It is noted that this force occurs due to a magnetic field perpendicular to the velocity vector.

$$F_D \propto \sigma u B_{\perp}^2 \quad (A.5)$$

For the waves investigated in the Liquid Metal eXperiment Upgrade (LMX-U) channel, the direction of wave propagation was chosen to be the x-direction. By examining wave-like perturbations in the fluid of the form  $\exp[i(kx - \omega t)]$  and applying pressure balancing conditions, a dispersion relation for MHD surface waves may be reached as shown in (A.6) [4].

than a spatial decay.

For a flowing liquid lithium divertor in the magnetic field conditions on tokamaks such as DIII-D and ITER ( $B_T \approx 2$  T,  $B_p \approx 0.08$  T, and  $B_T \approx 5$  T,  $B_p \approx 0.7$  T), the damping time scales range from  $2.7 \times 10^{-2}$  s to  $4.4 \times 10^{-5}$  s and  $3.9 \times 10^{-4}$  s to  $5 \times 10^{-6}$  s respectively for waves traveling in the poloidal and toroidal directions. While these predictions use the deep limit assumption, based on the damping found in the fringing field region on LMX-U these timescales can be projected to be approximately a factor of two shorter. Comparing these values to the flow exposure timescale of  $1 \times 10^{-2}$ , waves in the toroidal direction are quickly damped out while waves in the poloidal direction are damped relatively slowly. The growth rate of certain instabilities may outpace the damping rates enough that magnetic field can not be solely relied on to prevent the instabilities.

Future experiments on liquid metal divertor configurations with full axisymmetric flow are necessary to project to reactors because of their unique boundary conditions and ability to generate loop currents. In addition, the effects of externally injected electrical current may be examined more fully beyond the limitations of the LMX-U configuration. More studies may also be done in channel flow with conductive boundary conditions to more closely mimic actual LM-PFCs.

#### Acknowledgments

The authors would like to thank P. J. Vail and F. M. Laggner for their useful contributions and insights.

The research described in this paper was conducted under the Laboratory Directed Research and Development (LDRD) Program at Princeton Plasma Physics Laboratory, a national laboratory operated by Princeton University for the U.S. Department of Energy under Prime Contract No. DE-AC02-09CH11466.

This manuscript is based upon work supported by the U.S. Department of Energy, Office of Science, Office of Fusion Energy Sciences, and has been authored by Princeton University under Contract No. DE-AC02-09CH11466 with the U.S. Department of Energy.

The publisher, by accepting the article for publication, acknowledges that the United States Government retains a non-exclusive, paid-up, irrevocable, worldwide license to publish or reproduce the published form of this manuscript, or allow others to do so, for United States Government purposes.

Digital data for this paper can be found at:

<http://arks.princeton.edu/ark:/88435/dsp01x920g025r>.

$$\rho\omega^2 = (\rho g - j_{0z} B_x + k^2 T) k^2 \tanh(Kh) / K \quad (\text{A.6})$$

Where  $K^2 = k^2(1 - i\alpha)$  and  $\alpha = \sigma B_x^2 / (\rho\omega)$ . The influence of viscosity has been neglected here. It is noted that (A.6) does not include  $B_z$  or  $j_x$ , despite their interaction causing a vertical force on the flow as predicted on the right hand side of (A.2). A complete derivation and explanation of this is found by others [2,4]. The two limits that are commonly considered are the shallow and deep limits, and they are characterized by the behavior of the hyperbolic tangent term in the dispersion relation. A small depth to wavelength ratio exhibits shallow limit wave behavior, while a large depth to wavelength ratio exhibits deep limit wave behavior. When examining surface waves at the deep limit ( $kh > 1$ ,  $\tanh(kh) \approx 1$ ), the dispersion relation is given by (A.7).

$$\rho\omega^2 = (\rho g - j_{0z} B_x + k^2 T) k / \sqrt{1 - i\alpha} \quad (\text{A.7})$$

By splitting the wave number into a real and imaginary term ( $k = k_r + ik_i$ ), the convective damping rate may be found. Examining the imaginary component of the dispersion relation (A.7) leads to (A.8) with several additional assumptions ( $k_r \gg k_i$ , and  $\alpha < 1$ ) [4].

$$k_i = -\frac{\alpha \rho \omega^2 k_r}{2(\rho \omega^2 + 2T k_r^2)} \quad (\text{A.8})$$

At the shallow limit ( $kh < 1$ ,  $\tanh(kh) \approx kh$ ) the surface wave dispersion relation is given by (A.9) [4].

$$\rho\omega^2 = (\rho g - j_{0z} B_x + k^2 T) k^2 h \quad (\text{A.9})$$

Now, the term  $\alpha$  disappears and there is no longer damping predicted due to magnetic field in the absence of external currents. This suggests a significant challenge for proposed thin-film, fast-flowing liquid metal divertor configurations as fluid instabilities and splashing that develop from surface waves will not be damped so long as  $kh < 1$ .

## Supplementary material

Supplementary material associated with this article can be found, in the online version, at [10.1016/j.nme.2019.02.014](https://doi.org/10.1016/j.nme.2019.02.014).

## References

- [1] S. Chandrasekhar, *Hydrodynamic and Hydromagnetic Stability*, Dover Publications, 1981. (First published 1961)
- [2] J.A. Shercliff, Anisotropic surface waves under a vertical magnetic force, *J. Fluid Mech.* 38 (2) (1969) 353–364.
- [3] P. Fifiis, M. Christenson, M. Szott, K. Kalathiparambil, D.N. Ruzic, Free surface stability of liquid metal plasma facing components, *Nucl. Fusion* 56 (2016) 106020.
- [4] H. Ji, W. Fox, D. Pace, H.L. Rappaport, Study of magnetohydrodynamic surface waves on liquid gallium, *Phys. Plasmas* 12 (2005) 012102, <https://doi.org/10.1063/1.1822933>.
- [5] M. Jaworski, T. Abrams, J. Allain, M. Bell, R. Bell, A. Diallo, T. Gray, S. Gerhardt, R. Kaita, H. Kugel, B. LeBlanc, R. Maingi, A. McLean, J. Menard, R. Nygren, M. Ono, M. Podesta, A. Roquemore, S. Sabbagh, F. Scotti, C. Skinner, V. Soukhanovskii, D. Stotler, the NSTX Team, Liquid lithium divertor characteristics and plasma–material interactions in NSTX high-performance plasmas, *Nucl. Fusion* 53 (8) (2013) 083032.
- [6] N.B. Morley, J. Burris, The MTOR LM-MHD flow facility, and preliminary experimental investigation of thin layer, liquid metal flow in a 1/R toroidal magnetic field, *Fusion Sci. Technol.* 44 (2003) 74–78.
- [7] S.M.H. Mirhoseini, R. Diaz-Pacheco, F.A. Volpe, Passive and active electromagnetic stabilization of free-surface liquid metal flows, *Magnetohydrodynamics* 53 (2017) 1–10.
- [8] J. Yang, T. Qi, D. Ren, B. Liu, M. Ni, Surface waves of liquid metal film flow under the influence of spanwise magnetic field, *Fusion Eng. Des.* 130 (2018) 42–47.
- [9] Z.H. Wang, X. Jia, M.-J. Ni, Effect of the magnetic field and current orientation on the splashing of liquid metal free surface of fusion reactor PFCs, *Nucl. Fusion* 58 (2018) 126011, <https://doi.org/10.1088/1741-4326/aade0c>.
- [10] R.E. Nygren, F.L. Tabars, Liquid surfaces for plasma facing components—a critical review. Part i: physics and psi, *Nucl. Mater. Energy* 9 (2016) 6–21, <https://doi.org/10.1016/j.nme.2016.08.008>.
- [11] V. Surla, M.A. Jaworski, T.K. Gray, K. Ibane, W. Xu, M.J. Neumann, D.N. Ruzic, Lithium research as a plasma facing component material at the university of illinois, *Thin Solid Films* 518 (2010) 6663–6666, <https://doi.org/10.1016/j.tsf.2010.03.063>.
- [12] H.W. Davison, *Compilation of Thermophysical Properties of Liquid Lithium*, Technical Report, National Aeronautics and Space Administration, 1968.
- [13] A.E. Fisher, E. Kolemen, M.G. Hvasta, Experimental demonstration of hydraulic jump control in liquid metal channel flow using lorentz force, *Phys. Fluids* 30 (2018) 067104.
- [14] M.G. Hvasta, E. Kolemen, A.E. Fisher, H. Ji, Demonstrating electromagnetic control of free-surface, liquid-metal flows relevant to fusion reactors, *Nucl. Fusion* 58 (1) (2018) 016022.
- [15] D. Meeker, *Finite Element Method Magnetics, Version 4.2*, October, 2015.
- [16] S.M.H. Mirhoseini, F.A. Volpe, Resistive sensor and electromagnetic actuator for feedback stabilization of liquid metal walls in fusion reactors, *Plasma Phys. Controlled Fusion* 58 (1) (2016) 124005.
- [17] B. Lautrup, *Physics of Continuous Matter*, Institute of Physics Publishing, 2005.
- [18] M. Abdou, N.B. Morley, S. Smolentsov, A. Ying, S. Malang, A. Rowcliffe, M. Ulrickson, Blanket/first wall challenges and required R&D on the pathway to demo, *Fusion Eng. Des.* 100 (2015) 2–43.
- [19] N.B. Morley, S. Smolentsev, D. Gao, Modeling infinite/axisymmetric liquid metal magnetohydrodynamic free surface flows, *Fusion Eng. Des.* 63–64 (2002) 343–351.
- [20] L.E. Zakharov, Magnetic propulsion of intense lithium streams in a tokamak magnetic field, *Phys. Rev. Lett.* 90 (2003) 045001.